Removal of Zn(II), Mn(II) and Cu(II) by adsorption onto banana stalk biochar: adsorption process and mechanisms

Hua Deng, Qiuyan Li, Meijia Huang, Anyu Li, Junyu Zhang, Yafen Li, Shuangli Li, Caiyan Kang and Weiming Mo

ABSTRACT

Low-cost banana stalk (*Musa nana* Lour.) biochar was prepared using oxygen-limited pyrolysis (at 500 °C and used), to remove heavy metal ions (including Zn(II), Mn(II) and Cu(II)) from aqueous solution. Adsorption experiments showed that the initial solution pH affected the ability of the biochar to adsorb heavy metal ions in single- and polymetal systems. Compared to Mn(II) and Zn(II), the biochar exhibited highly selective Cu(II) adsorption. The adsorption kinetics of all three metal ions followed the pseudo-second-order kinetic equation. The isotherm data demonstrated the Langmuir model fit for Zn(II), Mn(II) and Cu(II). The results showed that the chemical adsorption of single molecules was the main heavy metal removal mechanism. The maximum adsorption capacities ($mg \cdot g^{-1}$) were ranked as Cu(II) (134.88) > Mn(II) (109.10) > Zn(II) (108.10)) by the single-metal adsorption isotherms at 298 K. Moreover, characterization analysis was performed using Fourier transform infrared spectroscopy, the Brunauer-Emmett-Teller method, scanning electron microscopy with energy-dispersive X-ray spectroscopy, X-ray diffraction, and X-ray photoelectron spectroscopy. The results revealed that ion exchange was likely crucial in Mn(II) and Zn(II) removal, while C-O, O-H and C = O possibly were key to Cu(II) removal by complexing or other reactions.

Key words | adsorption mechanisms, biochar, heavy metals, selective adsorption

HIGHLIGHTS

- The biochar showed strongly selective adsorption for Cu(II) in different pH.
- The major adsorption mechanisms of heavy metals were proposed.
- New insight for the selective mechanism of biochar for heavy metals was presented.

Hua Deng
Qiuyan Li
Meijia Huang
Anyu Li
Junyu Zhang
Yafen Li
Shuangli Li
Caiyan Kang (corresponding author)
Key Laboratory of Ecology of Rare and Endangered Species and Environmental Protection,
Guangxi Normal University,
Guilin 541004, China
and
College of Environment and Resources,
Guangxi Normal University,
Guilin 541004, China
E-mail: *309367585@qq.com*

Hua Deng
Qiuyan Li
Meijia Huang
Junyu Zhang
Yafen Li
Shuangli Li
Caiyan Kang
Key Laboratory of Karst Ecology and Environmental Change,
Guangxi Department of Education,
Guilin 541004, China

Weiming Mo
School of Chemistry and Pharmaceutical Science,
Guangxi Normal University,
Guilin 541004, China

doi: 10.2166/wst.2020.543

GRAPHICAL ABSTRACT

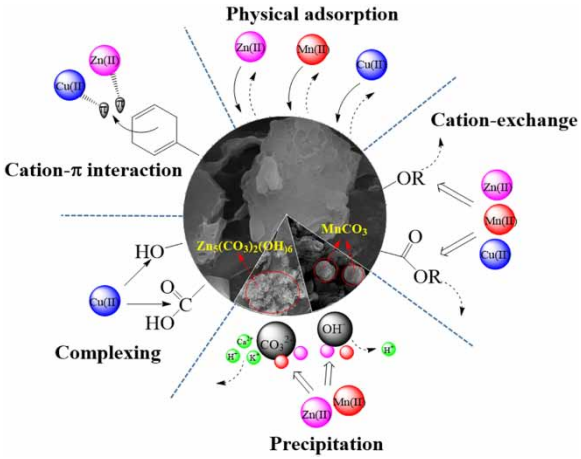

INTRODUCTION

In recent years, due to the acceleration of industrialization and urbanization, environmental pollution has become increasingly serious. In particular, heavy metal pollution, as a byproduct of rapid economic development, is widely encountered in many industrial wastewaters, as in nonferrous metal smelting, the electroplating industry, and in tailings. In China, the maximum allowable discharge level of copper, manganese and zinc is 5.0 $mg{\cdot}L^{-1}$ according to the Comprehensive Wastewater Discharge Standard (GB8978-1996, China). Heavy metals are toxic, transportable and nonbiodegradable, and can accumulate in organisms and even humans, seriously threatening human health and environmental safety. Copper, manganese and zinc are essential trace elements that play an important role in cartilage and bone formation, but excessive exposure to these metals is toxic to the central nervous system. A high level of Cu(II) can lead to high blood pressure, polycystic liver and kidney damage and diseases of the central nervous system (Wei *et al.* 2019). According to World Health Organization standards (Pietrelli *et al.* 2019), the maximum manganese content in drinking water should be 0.1 $mg{\cdot}L^{-1}$. Researchers have found that inhaling too much manganese can cause acute poisoning, so-called metal vapor poisoning. Chronic manganese poisoning can lead to headaches, emotional agitation, irritability, personality disorders, hallucinations, deafness, stiffness and tremors. According to Atangana (2019), zinc toxicity can cause human diseases such as dizziness, kidney disease, muscle weakness and stomach pain, all due to the presence of large amounts of zinc chloride. Therefore, it is very important to develop effective technology to mitigate heavy metal pollution.

A number of treatment techniques have been developed, including membrane separation, precipitation, ion exchange, chemical oxidation, and adsorption (Leiva *et al.* 2018; López *et al.* 2019; Murray & Ormeci 2019). Many of those methods require high operating and related costs and are prone to cause secondary pollution of the environment. In recent years, adsorption has been favored by researchers due to its low cost, environmental friendliness and high efficiency. Carbon materials such as activated carbon and biochar have been developed as adsorbents to remove heavy metal pollution (Divband Hafshejani *et al.* 2016). Biochar is more economical and easier to prepare than activated carbon. Biochar prepared by the oxygen-limited heating biomass results in a large number of microporous structures, a large surface area and abundant surface energy groups. For example, Peng (Peng *et al.* 2018), using Fourier transform infrared spectroscopy (FTIR), scanning electron microscopy (SEM) and energy-dispersive X-ray spectroscopy (EDS), confirmed that Si-O, O-S-O, C-O and C = O in millet shells were crucial to removing chromium, cadmium, zinc, and copper, respectively.

Bananas are perennial herbs and are one of the most traded fruits worldwide. Most bananas are produced in tropical countries and shipped to wholesale markets, where they are processed for distribution; as a result large

quantities of stalks are discarded as agricultural waste. To utilize these discarded resources, this study implemented the pyrolysis of agricultural waste to prepare biochar, which was used to remove heavy metal pollutants from aqueous solution. The objectives of this work are (1) to study the adsorption behavior of banana stalk biochar (BB) for single metals (Mn(II), Zn(II), and Cu(II)); (2) to compare and analyze the adsorption effects of mixed-metal solutions; and (3) to evaluate the adsorption mechanism by FTIR, X-ray photoelectron spectroscopy (XPS), the Brunauer-Emmett-Teller (BET) method, SEM-EDS, and X-ray diffraction (XRD).

MATERIALS AND METHODS

Biochar preparation

Banana stalks were collected from a farmers' market in Guilin, China. First, they were washed, then most of the moisture was removed, after which they were completely dried at 105 °C. Then, they were ground to powder, which was passed through a 0.250-mm sieve (60 mesh). Finally, the pretreated powder was calcined in a muffle furnace at 500 °C for 2 hours. The process is shown in Figure S1 (Supplementary Information).

Adsorption experiments

Stock solutions of copper, manganese, and zinc were prepared from cupric nitrate, manganese sulfate, and zinc nitrate, respectively. All static adsorption experiments were conducted in 150-mL conical bottles, whereby 0.1 g BB was mixed with 50 mL ion solution and oscillated at 150 rpm in a thermostatic oscillator. The influence of the pH on metal ion adsorption was measured by adding 0.1 M NaOH or HCl and adjusting the initial pH of the metal solution (200 $mg{\cdot}L^{-1}$) to 2.0–6.0. Competitive adsorption experiments were investigated with a variety of metal mixtures containing Mn(II), Zn(II), and Cu(II), in which the pH was adjusted in the range of 2.0–6.0 with the ion concentration of the solution being 200 $mg{\cdot}L^{-1}$.

Adsorption kinetics experiments were conducted with different durations (1–1,440 min), and the ion concentration of the solution was 200 $mg{\cdot}L^{-1}$. For the adsorption thermodynamics experiments, the initial solution concentration was designed to range from 100 to 600 $mg{\cdot}L^{-1}$, maintaining the initial solution pH unchanged, and the solution was oscillated at different temperatures (25 °C, 35 °C and 45 °C) for 240 min.

For adsorption-desorption experiments, 0.1 g BB was added to 50 mL, 200 $mg{\cdot}L^{-1}$ solution and shaken at 150 rpm for 240 min. The sample was filtered and dried. Then the dried sample was immersed in 0.1 M HCl, stirred magnetically for 240 min, and then filtered and dried. The above adsorption liquid was filtered through a 0.45 μm PTFE hydrophobic syringe, and the metal ion concentrations were measured by an atomic adsorption spectrometer. The adsorption value was calculated using the following equation:

$$Q = \frac{(C_0 - C_e) \cdot V}{m} \quad (1)$$

where m (g) is the biochar mass; C_0 and C_e ($mg{\cdot}L^{-1}$) represent the initial and equilibrium concentrations of the metal ions, respectively; and V (L) is the solution volume.

Biochar characterization

The characteristic functional groups on the sample surface were characterized by an FTIR instrument (Bruker Tensor 27, Ettlingen, Germany). The wavenumber accuracy was greater than 0.01 cm^{-1}, the range was 4,000–400 cm^{-1}, and the resolution was 0.09 cm^{-1}. The textural properties of the samples were analyzed using an automatic adsorption analyzer at 77 K on an ASAP 2460 surface area and porosimetry system (ASAP2020, Micromeritics, USA). The average pore size distribution, surface area and total pore volume were all calculated by the BET method. The surface morphology of biochar samples was observed by SEM with a rated scanning voltage of 20 kV (JEOL-6700, Japan). Elemental mapping analysis was conducted using EDS (Aztec X-Max 80, Oxford Instruments, UK). The crystal structure of the material was analyzed using an XRD instrument with Ni-filtered Cu Kα radiation in the range of 5°–80° (2θ) (Bruker D8 Advance, Germany). The surface elemental contents and functional groups were determined by XPS with Mg-Ka radiation emitted from a double anode at 50 W (Thermo Scientific K-Alpha, UK).

RESULTS AND DISCUSSION

Analysis of the pH

The pH of the solution is one of the important factors affecting adsorption performance. The pH can affect the deprotonation/protonation of functional groups, the heavy

metal ion speciation and the surface charge on the biochar surface, as well as the dissolution of mineral components (Chen *et al.* 2019). The influence of different initial pH values on the adsorption of three metal ions onto BB is shown in Figure 1. For single- and polymetal systems, the adsorption of heavy metals onto BB increased with increasing pH and then stabilized. At a solution pH of 2, a large number of H^+ ions compete with the heavy metal ions for the adsorption sites on the biochar surface. In addition, biochar releases a large amount of Ca^{2+}, Mg^{2+} and K^+ during adsorption, which compete with the heavy metal ions in solution, thereby inhibiting Mn(II), Zn(II) and Cu(II) adsorption (Qiu *et al.* 2019). With the increase of the pH of the solution, the metal ion hydrolysis (as shown in Equation (2)), and the degree of acid dissociation of the organic functional groups onto the adsorbent surface and the negative surface charge increase, resulting in increasing deprotonization of the functional groups and an enhanced adsorption capacity (Gao *et al.* 2019). At the different pH levels, the equilibrium pH increases with increasing initial pH, as shown in Figure 1(a) and 1(b). This may occur due to the addition of alkaline biochar. When the pH is higher than 5, the amount of metal ions adsorbed is not notably affected.

$$M^{2+} + H_2O \rightleftharpoons M(OH)^+ + H^+ (M = Cu, Mn, Zn) \quad (2)$$

Selective adsorption

The heavy metal adsorption in polymetal- and single systems was similar at different pH levels, and the adsorption capacity gradually increased with increasing pH. However, it was observed that the removal capacity of BB for the three metal ions changed (Figure 1(a) and 1(c)). The adsorption of Cu(II) decreased by approximately 0.64%, whereas that of Mn(II) and Zn(II) decreased by 72.19% and 26.98%, respectively. The selectivity of BB for Mn(II), Zn(II) and Cu(II) was further analyzed according to the distribution coefficient (K_d):

$$K_d = \frac{V \times (C_0 - C_e)}{m \times C_e} \quad (3)$$

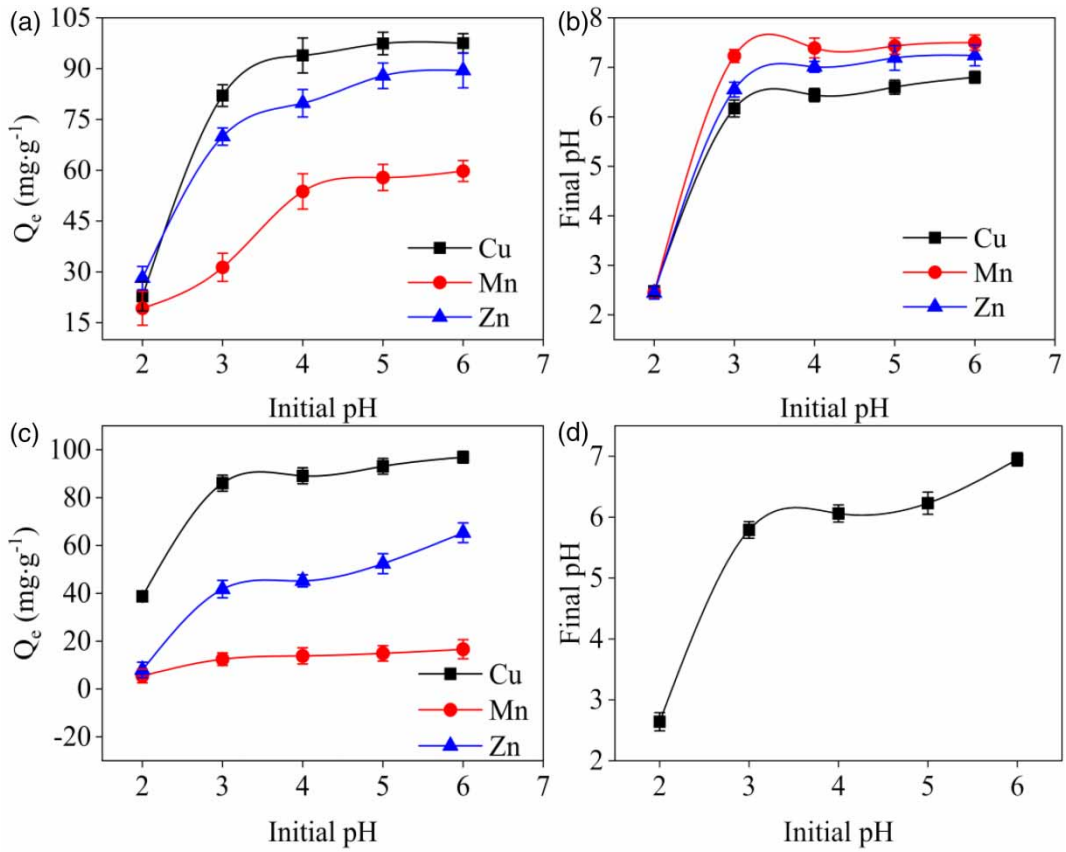

Figure 1 | Effect of initial solution pH on single metal adsorption (a), (b) and selective adsorption (c), (d) for BB.

where C_0 and C_e ($mg \cdot L^{-1}$) are the concentration of metal ions in the initial solution at equilibrium, respectively; m (g) is the biochar dosage; and V (L) is the solution volume.

The adsorbent selectivity coefficient in the presence of interference ions is defined by Equation (4) as:

$$\alpha = \frac{K_d(T)}{K_d(I)} \tag{4}$$

where $K_d(T)$ is the K_d value of the targeted metal (Cu(II) in this case), and $K_d(I)$ is the K_d value of the other metals in the polymetal solution (Mn(II) or Zn(II) here). A larger α value suggests a higher selectivity toward Cu(II) over either Mn(II) or Zn(II).

The K_d and α values of BB were calculated at different pH levels, as listed in Table 1. Clearly, the K_d value of Mn(II), Zn(II) and Cu(II) increased with increasing pH, and the α values also showed the same change trend. The increase in the K_d value can be explained by deprotonation. As the pH increases, more activated adsorption sites recovered, allowing more available metal ions to migrate from bulk solutions to the BB surface.

In addition, the selectivity of BB for Cu(II) over Mn(II) is significantly higher than for Cu(II) over Zn(II) at each pH.

Table 1 | Competitive binding behaviors of BB for Cu(II), Mn(II) and Zn(II) in mixed-metal system and various pH levels

pH	K_d(Cu)	K_d(Mn)	K_d(Zn)	α_{Mn}^{Cu}	α_{Zn}^{Cu}
2	0.147	0.1192	0.196	1.237	0.752
3	2.286	0.2283	1.164	10.01	1.964
4	7.697	0.5811	1.975	13.25	3.897
5	18.92	0.6869	3.632	27.54	5.208
6	19.5	0.743	4.234	26.24	4.606

According to the adsorption and α values, Cu(II) has a strong affinity for BB in a single-metal system, but notable adsorption inhibition is observed in a polymetal system. Oladipo *et al.* (2019) believe that the selectivity of metal ions in multicomponent systems is controlled by the electronegativity, size and hydration energy of the metal ions. For divalent metal ions, the difference can be ascribed to the different electronegativity (1.9 for Cu, and 1.65 for Zn and 1.55 for Mn) and mass-to-charge values (32 for Cu, and 33 for Zn and 27 for Mn) (Zhang *et al.* 2020). All these results indicate that BB has a higher adsorption capacity for Cu(II) than that for Mn and Zn(II), so BB has a higher selective adsorptivity for Cu(II).

Adsorption kinetics

Figure 2 showed the fitting results of BB adsorption kinetics for the three metals. The results revealed that the adsorption process of Mn(II), Zn(II) and Cu(II) can be divided between two steps. The first step was the rapid rise stage, which occurred mainly due to the initial stage of adsorption. The adsorbent surface adsorption sites were sufficient, which promoted adsorption. As the adsorption time increases, the adsorption sites on the adsorbent surface become occupied, and adsorption gradually approaches saturation and enters the equilibrium state. This stage is the slow adsorption stage. The adsorption of Mn(II) and Zn(II) onto BB increased slowly during the first stage (0–60 min) and then gradually reached equilibrium (60–1,440 min). However, the adsorption of Cu(II) onto BB increased almost exponentially during the first stage (0–15 min), and Cu(II) adsorption changed little during the second stage (15–1,440 min).

To understand the characteristics of the BB adsorption process, the pseudo-first-order kinetic and pseudo-second-order kinetic as well as intraparticle diffusion models were

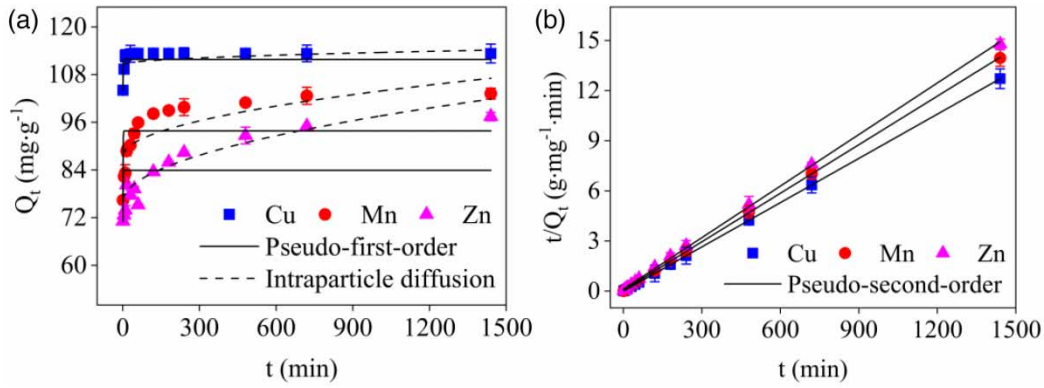

Figure 2 | Adsorption kinetics of BB in single metal systems.

fitted to the adsorption data of the three metals. The three adsorption models are given by following equations:

$$ln(Q_e - Q_t) = \ln Q_e - K_1 t \quad (5)$$

$$\frac{t}{Q_t} = \frac{1}{K_2 Q_e^2} + \frac{t}{Q_e} \quad (6)$$

$$Q_t = K_3 t^{1/2} + C \quad (7)$$

where Q_t and Q_e are the BB adsorption capacity at any time t and equilibrium time, respectively, the adsorption rate constants K_1 and K_2 are primary and secondary constants, respectively, K_3 is the diffusion constant in particles, C represents the thickness of the boundary layer, and T is the adsorption time; if Q_t is linear with $t^{1/2}$, and the curve passes through the origin of the coordinates, the control procedure is intraparticle diffusion.

According to the fitting results in Table 2, the fitting degree of the BB adsorption kinetics data for the three metals was quite different from that of the pseudo-first-order kinetic model, and R^2 was relatively small, indicating that the kinetic adsorption of the three metals onto BB was not suitable for the pseudo-first-order kinetic model. However, the pseudo-second-order kinetic model fits the adsorption kinetics for the three metals, and the correlation linearity exceeded 0.999, indicating that the adsorption process conforms to the pseudo-second-order kinetic model (Yang *et al.* 2019). Pseudo-second-order kinetics include all adsorption processes, i.e., external diffusion, surface adsorption diffusion and internal diffusion and more realistically reflects the adsorption of Mn(II), Zn(II) and Cu(II) onto the surface of BB (Fang *et al.* 2016).

The adsorption onto BB of the three metals was mainly chemical adsorption, but the adsorption rate control step may be controlled by the adsorbent from the outer surface of the adsorbent particles through the micropores onto the inner surfaces of the particles (Jiang *et al.* 2019). The parameters of fitted intraparticle diffusion indicate that there is no linear relationship between the Q_t and $t^{1/2}$ of the three metals, suggesting that the adsorption kinetics is controlled by other processes in addition to intraparticle diffusion.

Adsorption isotherms

The adsorption isotherms of the metal ions at concentrations of 100–600 mg·L^{-1} were studied. The equilibrium adsorption isotherms of the three metal ions were fitted to Langmuir (Equation (8)) and Freundlich (Equation (9)), respectively:

$$Q_e = \frac{K_L Q_m C_e}{1 + K_L C_e} \quad (8)$$

$$Q_e = K_F C^{1/n} \quad (9)$$

where Q_e is the adsorption amount at the adsorption equilibrium (mg·g^{-1}); K_L denotes the Langmuir constant (L·mg^{-1}); C_e represents the concentration of Mn(II), Zn(II) and Cu(II) at equilibrium (mg·L^{-1}); 1/n represents the Freundlich constant indicative of the adsorption intensity; and K_F is the adsorption coefficient.

Figure 3 shows that the adsorption amount of BB for the three metals increased with concentration and then gradually stabilized. Adsorption quickly increased at low concentrations, while at high concentrations, adsorption slowly increased. The corresponding fitting parameters are summarized in Table 3. The Langmuir fitting coefficient of BB for the three metal ions was clearly higher ($R^2 > 0.90$), indicating that the adsorption process was approximately monolayer adsorption, and most adsorbed substances were evenly distributed on the adsorbent surface to achieve adsorption saturation. In addition, Table 3 also indicates that BB attained the highest adsorption capacity for Cu(II), with the maximum adsorption amount reaching 143.19 mg·g^{-1}. Comparison of Mn(II), Zn(II) and Cu(II) adsorption by BB with other adsorbents is given in Table S1 (Supplementary Information). As indicated in Table S1, the adsorption capacity of BB to Cu(II)

Table 2 | Kinetic parameters of Cu(II), Mn(II) and Zn(II) onto BB in respective single metal system

	Pseudo-first-order model			Pseudo-second-order-model			Intraparticle diffusion model		
Metal ions	Q_e (mg·g^{-1})	K_1 (1·min^{-1})	R^2	Q_e (mg·g^{-1})	K_2 (mg·g·min^{-1})	R^2	C	K_t (mg·g^{-1}·min^{-1})	R^2
Cu(II)	112.92	2.543	0.8202	113.57	2.698	0.9999	111.004	0.102	0.1020
Mn(II)	94.80	1.633	0.2951	103.09	0.002	0.9999	85.714	0.635	0.6330
Zn(II)	83.50	1.902	0.0778	97.08	0.001	0.9995	73.489	0.750	0.8795

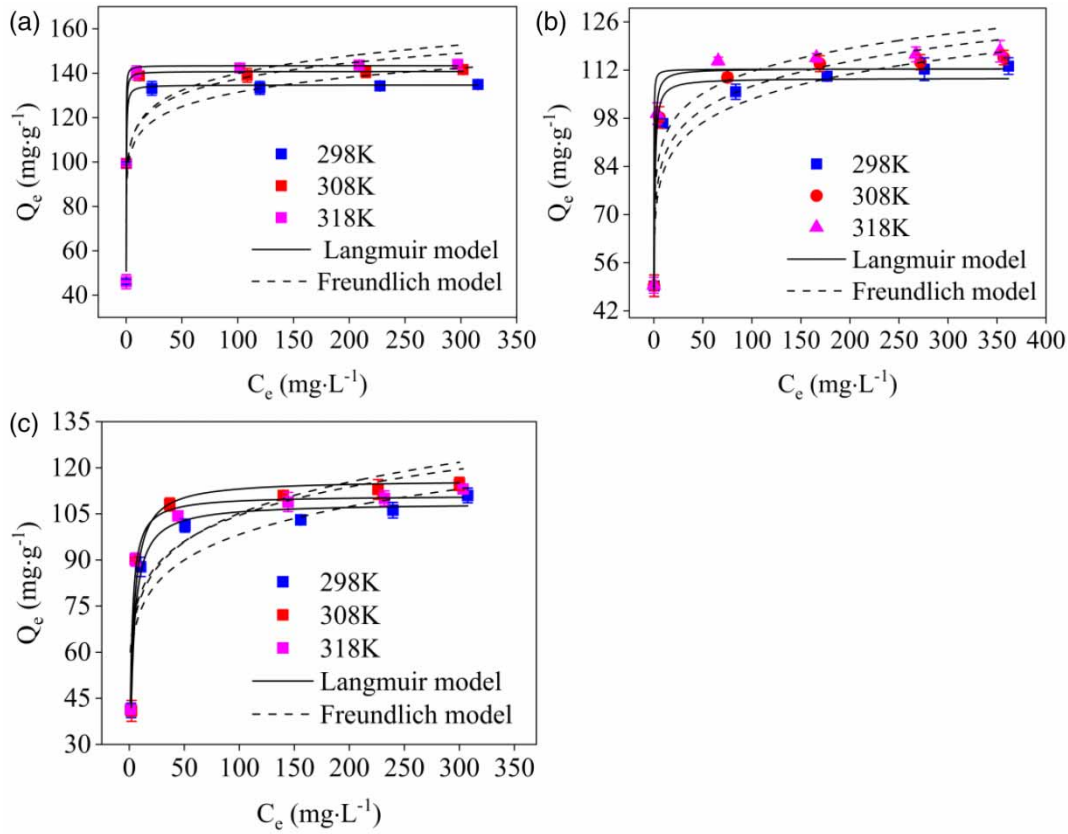

Figure 3 | Adsorption isotherms of Cu(a), Mn(b) and Zn(c) onto BB.

Table 3 | Langmuir and Freundlich isotherm parameters for adsorption of Cu(II), Mn(II), and Zn(II) onto BB

		Freundlich model			Langmuir model			
Metal ions	**T (K)**	**K_F (g·mg^{-1}·min^{-1})**	**n**	**R^2**	**1/K_L (mg·L^{-1})**	**Q_m (mg·g^{-1})**	**R^2**	**R_L**
Cu(II)	298	89.3978	12.2774	0.7068	0.1266	134.88	0.9712	0.0002–0.0013
	308	95.0654	12.5690	0.6825	0.0920	141.06	0.9469	0.0001–0.0009
	318	99.0917	13.1556	0.7221	0.0484	143.19	0.9903	0.0001–0.0005
Mn(II)	298	66.5827	10.3132	0.8492	0.4807	109.10	0.9620	0.0008–0.0048
	308	70.8992	11.0182	0.8220	0.3372	112.04	0.9675	0.0006–0.0034
	318	77.7074	12.7703	0.8504	0.0667	113.33	0.9385	0.0001–0.0007
Zn(II)	298	54.0167	7.6364	0.7587	2.7297	108.10	0.9874	0.0045–0.0266
	308	59.5961	8.0699	0.6502	2.5478	115.52	0.9215	0.0042–0.0248
	318	60.2083	8.4874	0.7355	1.6358	111.29	0.9869	0.0027–0.0161

(134.88 mg·g^{-1}) and Zn(II) (108.10 mg·g^{-1}) is higher than that of sesame straw biochar (Cu(II), 55.00 mg·g^{-1}; Zn(II), 34.00 mg·g^{-1}) and melon peel biochar (Cu(II), 79.36 mg·g^{-1}; Zn(II), 72.99 mg·g^{-1}), and the adsorption capacity of Mn(II) (109.10 mg·g^{-1}) is higher than that of poultry manure-derived biochar (2.84 mg·g^{-1}) and farmyard manure-derived biochar (6.65 mg·g^{-1}).

In addition, the adsorption efficiency of BB and other banana biochar was compared (Table S2, Supplementary Information). At the same initial concentration, dosage and solution conditions, the adsorption efficiency of banana peel biochar for Cu(II), Zn(II) and Hg(II) is 77.55%, 73.05% and 77.25%, respectively, and the adsorption efficiency of banana pseudostem biochar for Cr(VI) is

51.23%, which are lower than that of BB. These results show that BB has higher adsorption capacity and adsorption efficiency than other adsorbents and is therefore a promising adsorbent.

The dimensionless separation parameter R_L was adopted to estimate the favorability of metal ions sorption onto BB. The equation is as follows:

$$R_L = \frac{1}{1 + K_L C_0} \tag{10}$$

where R_L is affected by the initial concentration of the adsorbent solution. Effective adsorption is defined as $0 < R_L < 1$, with $R_L > 1$ defined as adverse adsorption. If $R_L = 0$, the adsorption is irreversible, and if $R_L = 1$, the adsorption is linear. In this study, the R_L value was maintained in the 0–1 range (Table 3), which indicated that the metal ions were effectively adsorbed onto the BB. The R_L value gradually decreased with increasing concentration, indicating that higher concentrations are beneficial to adsorption.

Cyclic adsorption of biochar

In order to explore the recyclability of biochar, 0.1 mol/L HCl was used as the desorption agent in this study. The cycling performance of desorbed biochar is shown in Figure 4. When the biochar was adsorbed for the first time, the removal rates of Zn(II), Mn(II) and Cu(II) were 95.64%, 81.43% and 99.5% respectively. After four times of cycling, the removal rates decreased to 53.15%, 48.5% and 74.31% respectively, indicating that the biochar has good cycling performance.

An important part of the research process is to apply the research results to the real world. In a previous study, we studied the adsorption performance of banana stem biochar on phosphorus by using actual pig wastewater (Jiang *et al.* 2020). In the next stage, we will take actual mine wastewater and electroplating wastewater as the research objects, and use the same method to study the adsorption performance of BB in the actual wastewater.

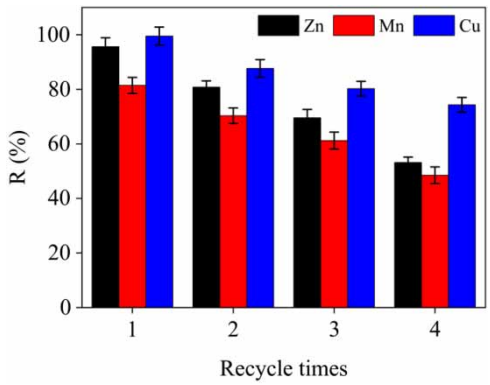

Figure 4 | Cycling studies of BB.

Adsorption mechanisms

BET analysis

BET tests were conducted to reveal the porosity and surface area of BB before and after adsorption of Mn(II), Zn(II) and Cu(II). The pore structure parameters are listed in Table 4. The specific surface area of biochar after Cu(II) adsorption increased from 4.68 to 33.34 $m^2 \cdot g^{-1}$, which means that it increased by more than seven times. At the same time, the specific surface areas of BB-Mn and BB-Zn increased to 53.09 and 41.38 $m^2 \cdot g^{-1}$, respectively, approximately 11.3 and 8.8 times, respectively, the level before adsorption. After adsorption, the total pore volume of the three materials increased, possibly because metal ions were adsorbed onto the surface of the materials, thereby increasing the specific surface area (Meng *et al.* 2018). After Cu(II) adsorption, the average pore size increased, which may occur because Cu(II) entered the interlayer channels of BB through intercalation during the adsorption process, thus widening the channels. Compared with that before adsorption, the average pore size of BB-Mn and BB-Zn decreased, which may have been caused by the metal ions being adsorbed during orifice or hole collapse in the adsorption process.

FTIR analysis

The FTIR spectra before and after the adsorption of Mn(II), Zn(II) and Cu(II) onto the biochar are shown in Figure 5. It is clear that the characteristic peak of BB had changed after adsorption of Mn(II), Zn(II) and Cu(II). The peak at 3,423 cm^{-1} was mainly generated by intermolecular

Table 4 | Pore structure parameters of BB before and after adsorption of Cu(II), Mn(II) and Zn(II)

Samples	BET surface area ($m^2 \cdot g^{-1}$)	Total pore volume ($cm^3 \cdot g^{-1}$)	Average pore size distribution (nm)
BB	4.68 ± 2.75	0.0149 ± 0.009	12.57 ± 0.32
BB-Cu	33.34 ± 7.33	0.1143 ± 0.0281	13.63 ± 0.38
BB-Mn	53.09 ± 3.25	0.0749 ± 0.0121	5.61 ± 0.57
BB-Zn	41.38 ± 3.02	0.1269 ± 0.0302	12.12 ± 2.03

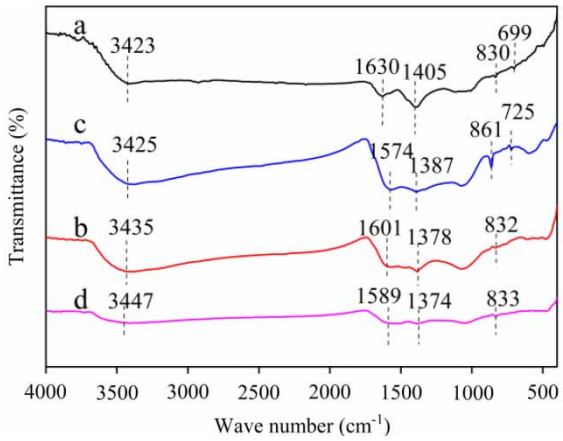

Figure 5 | FTIR spectra of biochar (a) before and after adsorption of Cu (b), Mn (c) and Zn (d).

hydrogen bond O-H stretching vibration, which provided a large amount of hydrogen bonding for metal ion adsorption. After the adsorption of Mn(II), Zn(II) and Cu(II), the characteristic peak migrated to 3,425, 3,435 and 3,447 cm^{-1}, respectively. Metal ions occupy -OH to a certain extent, thus reducing the molecular force of -OH. The peak at 1,630 cm^{-1} was mainly attributed to C = O and C = C stretching vibration of aromatic rings (Li *et al.* 2019). The wave band at 1,405 cm^{-1} may reflect the stretching vibration of -COO or the C = C skeleton vibration in aromatic hydrocarbons (Xu *et al.* 2018). It can be observed that the peak decreases and widens after adsorption, which may occur due to the hydrogen bonding provided by the adsorption of Mn(II), Zn(II) and Cu(II). The peak value at 830 cm^{-1} was Si-O-Si symmetric tensile vibration (Xu *et al.* 2018), the peak value at 699 cm^{-1} was the out-of-plane bending vibration of the C-H bond of the aromatic hydrocarbons (Oladipo *et al.* 2019), which disappeared after the adsorption of Zn(II) and Cu(II), indicating that the C-H bond on the biochar surface was involved in adsorption.

SEM-EDS analysis

The SEM-EDS patterns of the biochar before and after adsorption were analyzed and are presented in Figure 6. The SEM image reveals that the morphology of the biochar before adsorption exhibited irregular flakes with some small strips, which was significantly different from the biochar after adsorption. After Cu(II) adsorption, the biochar exhibited a loose and approximately rod-like structure. After adsorbing Mn(II), the surface resembled spherical crystals, and after the adsorption of Zn(II), flocculent substances with irregular shapes appeared on the biochar surface.

To understand the chemical composition of the biochar structure before and after adsorption, mapping characterization was performed at selected locations on the sample. The mapping diagram indicates that the C and K elemental content was reduced on the BB after adsorption of metal ions. The consumption of carboxyl hydroxyl groups on the biochar surface may be the reason for the decrease of the C elemental content. The reduction in K may be caused by the replacement of Mn(II), Zn(II) and Cu(II) in the solution during the adsorption process (Zhang *et al.* 2019). In the mapping diagrams in (b), (c), and (d), the corresponding Mn(II), Zn(II) and Cu(II) contents were measured after adsorption, indicating that the biochar had successfully adsorbed Mn(II), Zn(II) and Cu(II), respectively.

XRD analysis

Figure 7 shows the XRD patterns of BB (a), BB-Cu (b), BB-Mn (c) and BB-Zn (d). A Jade 6.0 phase search and comparison with JCPDS cards revealed that the fresh biochar contained $KHCO_3$ phases (PDF card 73–2155) at d = 7.27, 3.66, 2.96, 2.85, 2.62, 2.37, 2.28, 2.21, 2.03, 1.84, and 1.74 Å, indicating that the main crystalline phase of BB was $KHCO_3$. After Mn(II), Zn(II) and Cu(II) adsorption onto the biochar, the crystal shape had notably changed. After Mn(II) adsorption, the biochar had mainly formed MnO_2 (PDF card 29-0895) and $MnCO_3$ (PDF card 44-1472). $Zn_5(CO_3)_2(OH)_6$ (PDF card 19-1458) was formed after the adsorption of Zn(II), which may be the combination of biochar with metal ions through chemical coordination. Moreover, the characteristic peaks disappeared after Cu(II) adsorption. After the adsorption of Cu(II), the diffraction peaks were wide and stable without obvious crystallization peaks, indicating that the resulting products have a low crystallinity and may generate amorphous compounds.

XPS analysis

To further examine the adsorption mechanism, the biochar before and after heavy metal ion adsorption was analyzed by XPS. The XPS spectra of BB before and after heavy metal ion adsorption are shown in Figure 8. Figure 8(e) shows three new binding energies at 642, 935, and 1,023 eV, which were assigned to Mn 2p, Cu 2p, and Zn 2p photoelectrons, respectively, proving that Mn(II), Zn(II) and Cu(II), had been successfully adsorbed onto the biochar. In addition, the BB full-scan spectra

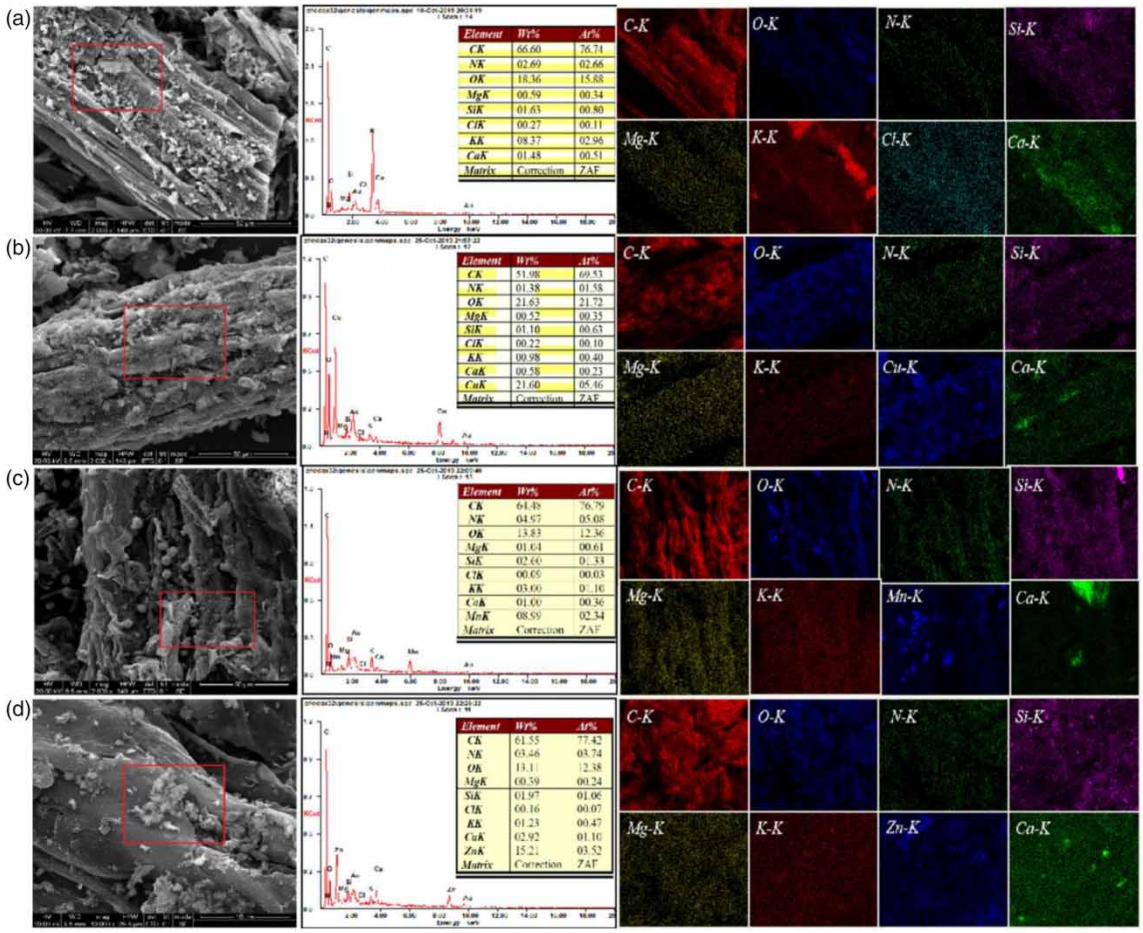

Figure 6 | SEM mapping of BB (a), BB-Cu (b), BB-Mn (c) and BB-Zn (d).

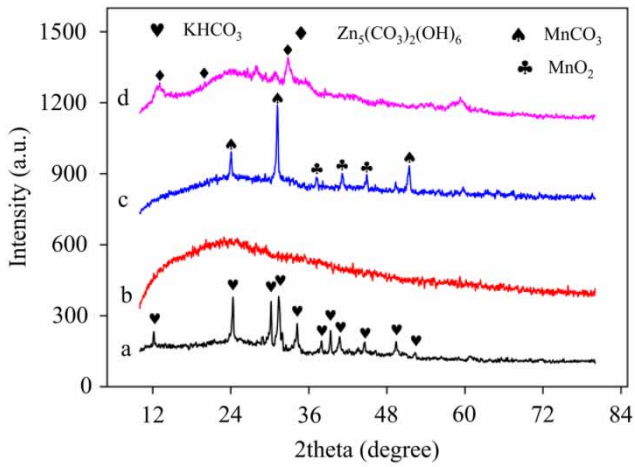

Figure 7 | XRD analysis of biochar (a) before and after adsorption of Cu (b), Mn (c) and Zn (d).

reflected the elimination of potassium after adsorbing heavy metal ions, which indicated that heavy metal ion adsorption was partly due to ion exchange. Figure 8(a)–8(d) show the high-resolution C1s XPS spectra of the biochar before and after heavy metal adsorption (Li *et al.* 2020). The C1s spectra of the biochar can be divided into three peaks at 284.80, 285.65, and 288.54 eV, which were attributed to C-C, C-O and C = O, respectively. After the adsorption reaction, the peaks of C-O and C = O notably changed and move towards higher binding energies. The formation of metal complexes may be the main reason for the shift in these peaks. For the biochar before adsorption, the O1s signal could be attributed to three different environments: O-M (metal) at approximately 530.92 eV (Lan *et al.* 2019), C-O or O-H at approximately 531.42 eV (Almeida *et al.* 2012), and C = O bonds at approximately 532.48 eV (Guo *et al.* 2018). The specific peaks of C-O or O-H shifted to a higher intensity and the oxygen atomic content of C = O decreased from 35.94% to 15.71% after copper adsorption (Figure 8(a′) and 8(b′)). This finding indicated that C-O, O-H, and C = O were likely important and effective functional groups for copper removal

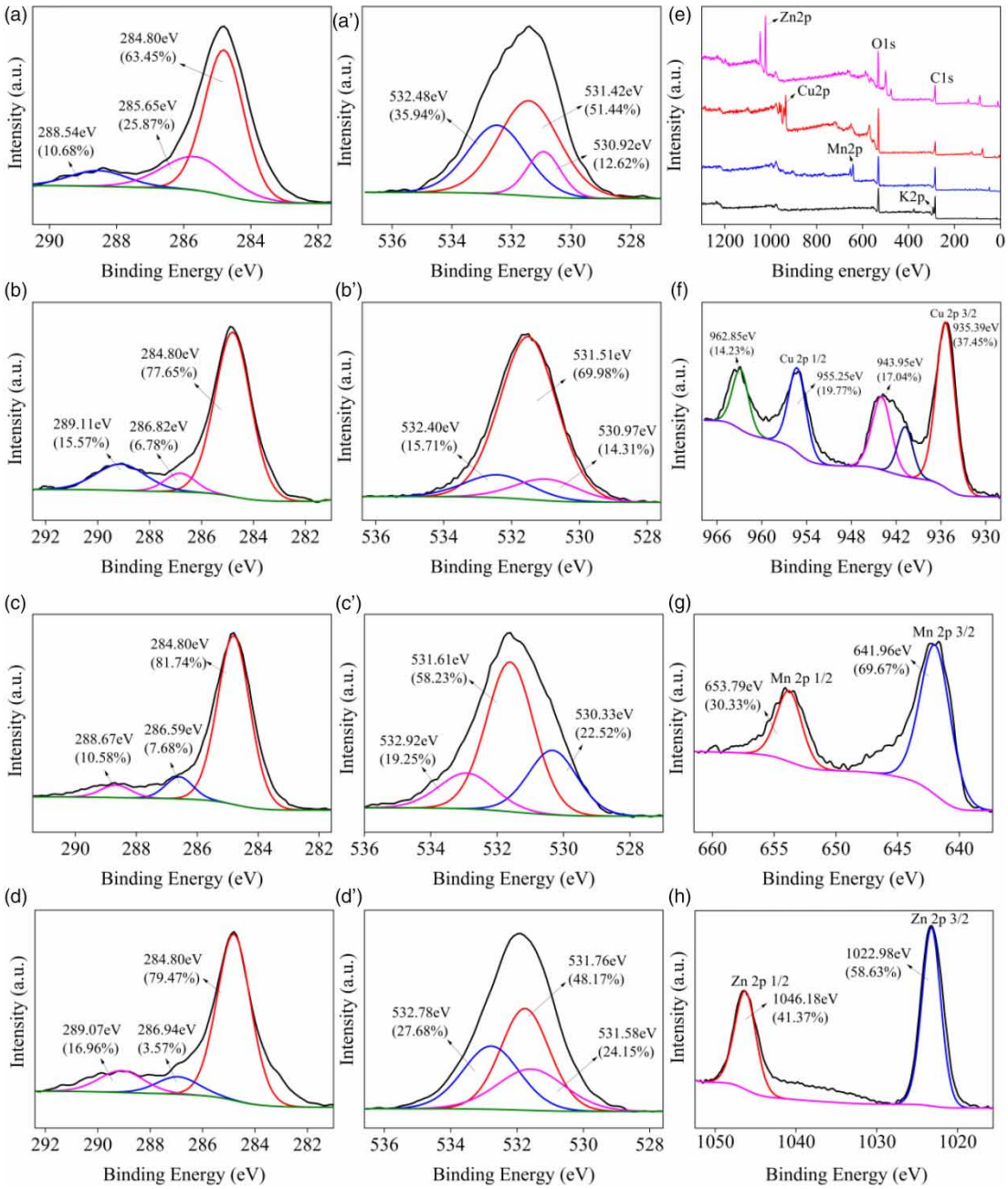

Figure 8 | The survey scan XPS spectra (e) and high-resolution scan XPS spectra of C1s (a, b, c, d), O1s (a′, b′, c′, d′), Cu 2p (f), Mn 2p (g) and Zn 2p (h).

(Lan *et al.* 2019). In addition, the characteristic peak of the Cu 2p3/2 at approximately 935.39 eV (Figure 8(f)) indicated the presence of Cu(II) hydroxides (Cu 2p3/2 at 935.1 eV) (Li *et al.* 2020). The specific O-M (metal) peaks notably changed after Mn(II) and Zn(II) adsorption (Figure 8 (c′)-(d′)). The oxygen atomic content increased from 12.62% to 22.52% and 24.15%, respectively. This may be caused by the exchange of Mn(II) and Zn(II) with the lighter metal ion of O-M (mainly K^+) in the biochar to form O-Mn or O-Zn (Lan *et al.* 2019). In addition, peaks were observed at a binding energy of 1,022 eV, indicating Zn 2p3/2 in biochar (Figure 8(h)), which suggested that the main species of Zn(II) was ZnO (Bogusz *et al.* 2015). The Mn 2p3/2 peak appears at approximately 641.96 eV, and the spin energy separation is 11.8 eV (Figure 8(g)), indicating that the main species of Mn(II) was MnO_2 (Han *et al.* 2006). Song *et al.* suggested that MnO_2 could interact strongly with Cu ions

(Song *et al.* 2014), which was likely the reason why Cu(II) removal was faster than Zn(II) or Mn(II) removal.

CONCLUSIONS

In this work, discarded banana stalks were used to prepare biochar for the removal of heavy metal ions from aqueous solution. The adsorption experiments indicated that BB had a high selective adsorption ability for Cu(II) in polymetal systems at different pH values. The pseudo-second-order kinetic and Langmuir models suitably describe the adsorption kinetics and thermodynamics, respectively, indicating that BB adsorbed Zn(II), Mn(II) and Cu(II) mainly via monolayer chemical adsorption. Moreover, through characterization analysis, C-O, O-H and C = O in the biochar may be crucial to copper removal, while Mn(II) and Zn(II) mainly form O-Mn and O-Zn, respectively, by exchange with the lighter metal ions in the biochar. The current work enhances the comprehension of the adsorption differences between different heavy metal ions onto biochar, which is important for future research on the selective mechanism of modified biochar for specific heavy metal ions.

FUNDING INFORMATION

This work was partially supported by the National Natural Science Foundation of China (No. 41301343) and the Key Laboratory of Ecology of Rare and Endangered Species and Environmental Protection (Guangxi Normal University) (ERESEP2019Z07).

DATA AVAILABILITY STATEMENT

All relevant data are included in the paper or its Supplementary Information.

REFERENCES

Almeida, K. A., Landers, R. & Cardoso, D. 2012 Properties of faujasite zeolites containing methyl-substituted ammonium cations. *J. Catal* **294**, 151–160.

Atangana, E. 2019 Adsorption of Zn(II) and Pb(II) ions from aqueous solution using chitosan cross-linked formaldehyde adsorbent to protect the environment. *J. Polym. Environ.* **27** (10), 2281–2291.

Bogusz, A., Oleszczuk, P. & Dobrowolski, R. 2015 Application of laboratory prepared and commercially available biochars to adsorption of cadmium, copper and zinc ions from water. *Bioresour. Technol.* **196**, 540–549.

Chen, H., Li, W., Wang, J., Xu, H., Liu, Y., Zhang, Z., Li, Y. & Zhang, Y. 2019 Adsorption of cadmium and lead ions by phosphoric acid-modified biochar generated from chicken feather: selective adsorption and influence of dissolved organic matter. *Bioresour. Technol.* **292**, 121948.

Divband Hafshejani, L., Hooshmand, A., Naseri, A. A., Mohammadi, A. S., Abbasi, F. & Bhatnagar, A. 2016 Removal of nitrate from aqueous solution by modified sugarcane bagasse biochar. *Ecol. Eng.* **95**, 101–111.

Fang, Y., Wang, H., Yu, H. & Peng, F. 2016 From chicken feather to nitrogen and sulfur co-doped large surface bio-carbon flocs: an efficient electrocatalyst for oxygen reduction reaction. *Electrochim. Acta* **213**, 273–282.

Gao, L. Y., Deng, J. H., Huang, G. F., Li, K., Cai, K. Z., Liu, Y. & Huang, F. 2019 Relative distribution of Cd^{2+} adsorption mechanisms on biochars derived from rice straw and sewage sludge. *Bioresour. Technol.* **272**, 114–122.

Guo, S., Dan, Z., Duan, N., Chen, G., Gao, W. & Zhao, W. 2018 Zn(II), Pb(II), and Cd(II) adsorption from aqueous solution by magnetic silica gel: preparation, characterization, and adsorption. *Environ. Sci. Pollut. Res.* **25** (31), 30938–30948.

Han, R., Zou, W., Zhang, Z., Shi, J. & Yang, J. 2006 Removal of copper(II) and lead(II) from aqueous solution by manganese oxide coated sand. *J. Hazard. Mater.* **137** (1), 384–395.

Jiang, Y. H., Li, A. Y., Deng, H., Ye, C. H. & Huang, H. L. 2020 Adsorption property of phosphorus by magnesium-loaded banana stem biochar from swine wastewater. *Technol. Water Treat. (in Chinese)* **46** (06), 33–38 + 44.

Jiang, Y. H., Li, A. Y., Deng, H., Ye, C. H., Wu, Y. Q., Linmu, Y. D. & Hang, H. L. 2019 Characteristics of nitrogen and phosphorus adsorption by Mg-loaded biochar from different feedstocks. *Bioresour. Technol.* **276**, 183–189.

Lan, T., Li, P., Rehman, F. U., Li, X., Yang, W. & Guo, S. 2019 Efficient adsorption of Cd^{2+} from aqueous solution using metakaolin geopolymers. *Environ. Sci. Pollut. Res.* **26** (32), 33555–33567.

Leiva, E., Leiva-Aravena, E., Rodriguez, C., Serrano, J. & Vargas, I. 2018 Arsenic removal mediated by acidic pH neutralization and iron precipitation in microbial fuel cells. *Sci. Total Environ.* **645**, 471–481.

Li, M., Wei, D., Liu, T., Liu, Y., Yan, L., Wei, Q., Du, B. & Xu, W. 2019 EDTA functionalized magnetic biochar for Pb(II) removal: adsorption performance, mechanism and SVM model prediction. *Sep. Purif. Technol.* **227**, 115696.

Li, Z., Li, M., Wang, Z. & Liu, X. 2020 Coadsorption of Cu(II) and tylosin/sulfamethoxazole on biochar stabilized by nano-hydroxyapatite in aqueous environment. *Chem. Eng. J.* **381**, 122785.

López, J., Reig, M., Gibert, O. & Cortina, J. L. 2019 Increasing sustainability on the metallurgical industry by integration of membrane nanofiltration processes: acid recovery. *Sep. Purif. Technol.* **226**, 267–277.

Meng, Y., Zhang, X., Pan, G., Xia, S. & Ni, Z. 2018 Orthogonal synthesis of a novel hybrid layered material containing three different zincous components and its photocatalytic property investigation. *J. Hazard. Mater.* **350**, 144–153.

Murray, A. & Ormeci, B. 2019 Use of polymeric sub-micron ion-exchange resins for removal of lead, copper, zinc, and nickel from natural waters. *J. Environ. Sci. (China)* **75**, 247–254.

Oladipo, A. A., Ahaka, E. O. & Gazi, M. 2019 High adsorptive potential of calcined magnetic biochar derived from banana peels for Cu^{2+}, Hg^{2+}, and Zn^{2+} ions removal in single and ternary systems. *Environ. Sci. Pollut. Res.* **26** (31), 31887–31899.

Peng, S. H., Wang, R., Yang, L. Z., He, L., He, X. & Liu, X. 2018 Biosorption of copper, zinc, cadmium and chromium ions from aqueous solution by natural foxtail millet shell. *Ecotoxicol. Environ. Saf.* **165**, 61–69.

Pietrelli, L., Ippolito, N. M., Ferro, S., Dovi, V. G. & Vocciante, M. 2019 Removal of Mn and As from drinking water by red mud and pyrolusite. *J. Environ. Manage.* **237**, 526–533.

Qiu, Y., Zhang, Q., Li, M., Fan, Z., Sang, W., Xie, C. & Niu, D. 2019 Adsorption of Cd(II) from aqueous solutions by modified biochars: comparison of modification methods. *Water Air Soil Pollut.* **230**, 84.

Song, Z., Lian, F., Yu, Z., Zhu, L., Xing, B. & Qiu, W. 2014 Synthesis and characterization of a novel MnOx-loaded biochar and its adsorption properties for Cu^{2+} in aqueous solution. *Chem. Eng. J.* **242**, 36–42.

Wei, P., Zhu, Z., Song, R., Li, Z. & Chen, C. 2019 An ion-imprinted sensor based on chitosan-graphene oxide composite polymer modified glassy carbon electrode for environmental sensing application. *Electrochim. Acta.* **317**, 93–101.

Xu, S., Yu, W., Liu, S., Xu, C., Li, J. & Zhang, Y. 2018 Adsorption of hexavalent chromium using banana pseudostem biochar and its mechanism. *Sustainability* **10**, 4250.

Yang, F., Zhang, S., Cho, D. W., Du, Q., Song, J. & Tsang, D. C. W. 2019 Porous biochar composite assembled with ternary needle-like iron-manganese-sulphur hybrids for high-efficiency lead removal. *Bioresour. Technol.* **272**, 415–420.

Zhang, J., Shao, J., Jin, Q., Li, Z., Zhang, X., Chen, Y., Zhang, S. & Chen, H. 2019 Sludge-based biochar activation to enhance Pb(II) adsorption. *Fuel* **252**, 101–108.

Zhang, W., Song, J., He, Q., Wang, H., Lyu, W., Feng, H., Xiong, W., Guo, W., Wu, J. & Chen, L. 2020 Novel pectin based composite hydrogel derived from grapefruit peel for enhanced Cu(II) removal. *J. Hazard. Mater.* **384**, 121445.

First received 1 June 2020; accepted in revised form 27 October 2020. Available online 10 November 2020